Fuel 324 (2022) 124716

Contents lists available at ScienceDirect

Fuel

journal homepage: www.elsevier.com/locate/fuel

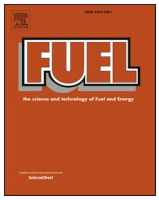

Full Length Article

A quantitative study of salinity effect on water diffusion in n-alkane phases: From pore-scale experiments to molecular dynamic simulation

Lifei Yan [a], Yuanhao Chang [b,*], S. Majid Hassanizadeh [a], Senbo Xiao [b], Amir Raoof [a,*], Carl Fredrik Berg [c], Jianying He [b]

[a] Department of Earth Sciences, Environmental Hydrogeology Group, Utrecht University, Utrecht 3584 CB, the Netherlands
[b] NTNU Nanomechanical Lab, Department of Structural Engineering, Norwegian University of Science and Technology (NTNU), Trondheim 7491, Norway
[c] Department of Geoscience and Petroleum, Norwegian University of Science and Technology (NTNU), S. P. Andersens veg 15, Trondheim 7031, Norway

ARTICLE INFO

Keywords:
Water diffusion
Water-alkane interface
Salinity effect
Microfluidic experiments
Molecular dynamic simulation

ABSTRACT

Numerous mechanisms have been proposed to untangle the effect of a low concentration of dissolved salts in the water flooding medium. One potential mechanism for enhanced oil movement is proposed with osmosis effect, however, the process of water transport through the oil phase, due to a salinity contrast, is not fully understood. In our study, we used three aqueous solutions and two alkanes in a series of microfluidic experiments with hydrophobically coated glass micro-chips for mimicking the low-salinity waterflooding process in an oil-wet rock formation. We created multiple systems of low-salinity water-alkane/high-salinity water in the porous micromodel, and afterward, continuously monitored the domain for 70 h. We noted that ionic strength and the hydrocarbon chain length both played important roles in water diffusion. A salinity contrast of 1.7 g/L-170 g/L caused a higher water volumetric flux than 50 g/L-170 g/L for both alkanes. The difference in water volumetric fluxes for those two contrasts were not proportional to the salinity contrast during the experimental period. There was no simple relationship between the chain length of hydrocarbon and water volumetric flux. Moreover, to investigate the effect of salinity on water behavior in heptane, we conducted molecular dynamic (MD) simulations by considering three different concentrations in the high-salinity water region featuring our experiments. The results indicated that high salinity limited the water diffusion from high-salinity phase into the oil phase and reduced the possibility of water entering the heptane phase. Therefore, the net flux of water from the pure water side to the salty waterside was enhanced.

1. Introduction

In the petroleum industry, low-salinity water flooding (LSWF) has been considered as a relatively effective low-cost engineering technique for enhanced oil recovery, compared with other chemical injection methods [1]. In recent decades, extensive laboratory studies (but not all) [2–4] and some field tests [5,6] have shown that the tertiary low salinity waterflooding gives better oil recovery performance in sandstone and carbonate reservoirs than conventional waterflooding with pure water or high-salinity water. Nevertheless, field data validating increased oil recovery by low-Sal injection is still limited. Thyne and Gamage [7] evaluated the potential for low-salinity waterflooding in the Minnelusa Formation in the Powder River Basin of Wyoming. They concluded that little or no incremental recovery from the low-salinity injection. Among the investigated 51 fields, 23 fields found no significant difference in the analysis of water breakthrough timing and water cut evolution between fields with low-salinity injection and mixed-water or saline injection. More than ten underlying mechanisms have been proposed for explaining the low-salinity effect and its contribution to oil displacement [8–10]. Currently, there is no consensus on a single mechanism governing this effect. Some of the mechanisms found in the literature are: (1) fines migration and mobilization [11], (2) wettability alteration [12], (3) reduced interfacial tension and increased pH effect [13,14], (4) multi-component ion exchange (MIE) [15], (5) double layer expansion [16], (6) emulsification and micro-dispersion [17] and (7) osmotic pressure [18]. Among the above-listed mechanisms, wettability alteration is believed to be the main factor for improving oil recovery, but the underlying cause is still unknown. The complexity of oil-brine (liquid-liquid) and/or rock-brine-oil (solid-liquid) interactions brings challenges to determining mechanisms and quantifying their effects [19],

* Corresponding authors.
E-mail addresses: Yuanhao.chang@ntnu.no (Y. Chang), A.Raoof@uu.nl (A. Raoof).

https://doi.org/10.1016/j.fuel.2022.124716
Received 11 March 2022; Received in revised form 16 May 2022; Accepted 28 May 2022
Available online 2 June 2022

and can also cause various counter observations from one suggested mechanism to another. Besides, the mechanism of osmosis is independent on influence of wettability alteration for explanation residue oil motion. Therefore, we don't discuss the mechanism of wettability alteration in this work. The aim of this study is to help deep understanding of "osmosis" mechanism and its contribution to oil movement during low-salinity waterflooding.

For fluid-solid interactions, Schmatz, et al. [20] acquired nano-scale imaging of oil-water-rock contact using cryogenic broad ion-beam polishing in combination with scanning electron microscopy. They observed that the non-wetting hydrocarbon phase is commonly separated from the rock by a thin brine film with local pinning at geometric and chemical heterogeneities. As a result of this situation, the injection of low-salinity water into a formation containing high-salinity water can cause the expansion of such thin brine films due to ionic diffusion [21]. Mahani, et al. [22] observed the detachment of crude oil droplets from the clay deposited glass substrate and described the kinetics of the low-salinity effect. Later on, they simulated the ionic transport using the coupled model of Nernst-Planck and Poisson equations and analysed dynamics of pressure field evolution inside thin brine films under the effect of ionic strength gradient. Recently, Aseyednezhad, et al. [23] simulated the same system but using a novel 1-dimensional model. Bartels, et al. [24] conducted a series of microfluidic experiments with single sinusoidal channel micro-models functionalized with clay particles and captured the de-wetting process during a tertiary low-salinity injection. They considered the formation and expansion of a high-salinity water film along the solid substrate as a pore-scale mechanism for the low-salinity effect. Moreover, core-flooding experiments using micro-CT tomography have proved that pore structure, the forms of residual oil patterns (e.g., types of isolated, cluster, network, and film) and even surfactant adsorption have significant effect on enhanced oil recovery during low-salinity injection [25–27].

On the other hand, some researchers highlighted that the effect of salinity on the water-oil interactions, i.e., osmosis, micro-emulsions, interfacial viscoelasticity, and use of non-ionic surfactant, have been overlooked in these studies [28–31]. Salinity may influence local water-oil interfacial properties and pressure, which ultimately affect oil ganglion dynamics, droplets coalescence and oil phase connectivity. Rücker, et al. [32] imaged the dynamic transient process of mobile oil ganglion induced by water film swelling by using X-ray computed micro-tomography. They found that mass transfer in the oil phase was accompanied by the meniscus oscillation and coalescence processes. Ayirala, et al. [33] experimentally investigated the microscopic-scale water ion interactions occurring at the crude-oil/brine interface under various salinity conditions. They noticed that the addition of salts could promote the transfer of surface-active components in the crude oil from the bulk phase into the interface. The sulfates-only brine showed the highest viscous and elastic moduli for the interfacial layers, meaning that addition of salt could significantly change the dynamic interface viscosities. Although the salinity effect has been confirmed by diverse experiments, the direct observations of the effect and a plausible explanation of mass transfer in oil are rarely reported. In the theory of osmosis, the chemical potential difference between two sides of a semi-membrane drives a net passage of water to the side being more saline, whereas the dissolved ions are excluded in such transport. Osmotic flow ceases when the aqueous activities of the two solutions on both sides of the membrane are the same, i.e., when the two water regions have reached the same salinity. In the analysis of oil displacement, some researchers believe that crude oil can be treated as a semi-permeable liquid membrane. Fredriksen, et al. [34] investigated the osmosis effect on water transport through the oil phase (functioning as a semi-permeable membrane) from a low salinity solution towards a high salinity solution using capillary experiments, core-flooding experiments, and 2D micro-model experiments. They observed the trapped HSW water swelling in the long period of brine-oil contact under salinity contrasts and obvious oil remobilization during low-salinity water flooding. Crestel, et al. [35] conducted experiments in two microfluidic systems, one with glass capillary and another with microfabricated cavities, for probing the oil motion on a solid substrate immersed in water. They observed the oil globule motion in confined systems and calculated the water flux induced by the theoretical osmotic pressure. In the long-term development for oil reservoirs, water diffusion through the oil phase could perform a considerable contribution to residual oil remigration for enhanced oil recovery.

Regarding the micro-dispersion/emulsion process, Emadi and Sohrabi [17] employed micro-models to observe interactions between crude oil and saline water. They noticed the formation of water micro-droplets in the crude oil phase when crude oil contacted with low-salinity water, which caused the expansion of connate water and residual oil redistribution. Du, et al. [36] captured the dynamic behavior of trapped oil dewetting and swelling during water flooding in micromodels with a single dead-end pore and observed the generation of micro-emulsions inside the swelling oil phase. They explained the phenomenon of oil swelling and micro-emulsions with a theory of water diffusion through crude oil low-salinity water towards high-salinity water. Yan, et al. [37] performed sets of capillary experiments capturing the movement of constrained oil globules induced by salinity contrast and 3D images of LSW-oil and HSW-oil interfaces for monitoring the dynamic contact angle change during oil movement. They proposed a hypothesis that water can be transported through crude oil via water diffusion and water-in-oil emulsions.

From the mentioned literature, there are two primary explanations for oil motion due to a salinity contrast: water diffusion through water films (formed between oil phase and pore walls) resulting in film expansion along water-wet rock surfaces (Fig. 1a) and water transport through oil phases (Fig. 1b). Note that here we do not consider the chemical reactions between fluids and minerals and the roughness in real rocks. The former mechanism (i.e., water diffusion into HSW film) comes about when the thin HSW film is directly exposed to an LSW environment. In other words, the solid substrate needs to be water-wet and the HSW area should not be blocked by the oil phase. In nature, HSW is commonly original at the residual state in a green oil reservoir. In this situation, the second mechanism (i.e., water diffusion through oil phase) becomes sensible for explaining the HSW expansion. Consequently, the research questions could be whether the oil phase can be treated as a membrane and what causes the water diffusion through the squeezed oil phase.

Although some works, e.g., Sandengen, et al. [28], have shown the swelling phenomenon of individual water droplets in a pure oil phase by osmotic-like flow, it is difficult to attribute this behavior to osmosis without further research. Also, in literature, the two processes of conventional osmosis and water diffusion in the oil phase are often mixed. Classically, the membrane considered in osmosis, e.g., biological, synthetic, or polymeric membrane, is normally insoluble to the aqueous phase. Lakshminarayanaiah and White [38] conducted experiments on water flow through solid polymeric and nonaqueous liquid membranes and found that the process of water transport through a rigid membrane physically differs from that through a liquid membrane. In the case of the solid membranes, e.g., an hollow fiber polyamide membrane [39], water flow is driven by the osmotic force from pure water to the saline water compartment and the pathway depends on the porous membrane properties, such as pore radius, permeability, and surface electrical behavior. In the case of organic liquid membranes, water diffusion is described as the motion of a species by means of kinetic jumps into neighboring vacancies, where the water pathway cannot be defined because of the kinetic motion of all molecules. Even though the phenomenon of salt solution expansion may look like osmosis under a macroscale observation, the organic phase cannot be treated as a rigid membrane.

On the other hand, the hydrocarbon layer thickness in organic liquids and salinity in aqueous solutions play an important role in the water solubility in hydrocarbon liquids [40], especially in crude oil containing

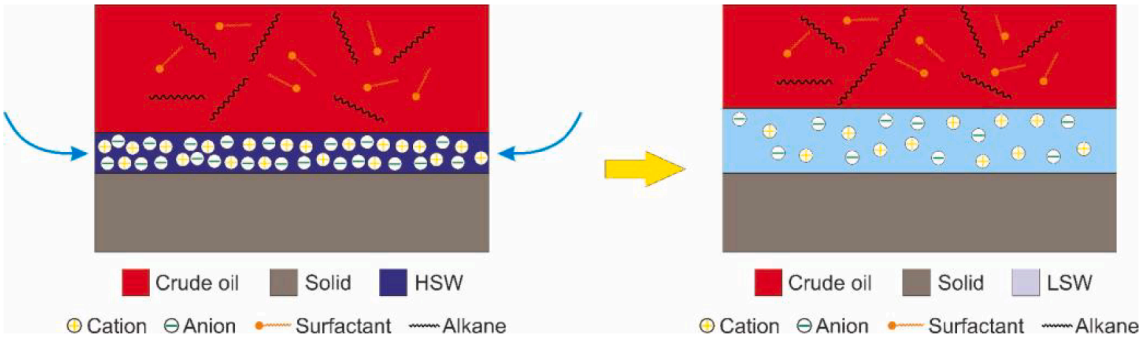

(a) water diffusion through a water film before and after LSW flooding

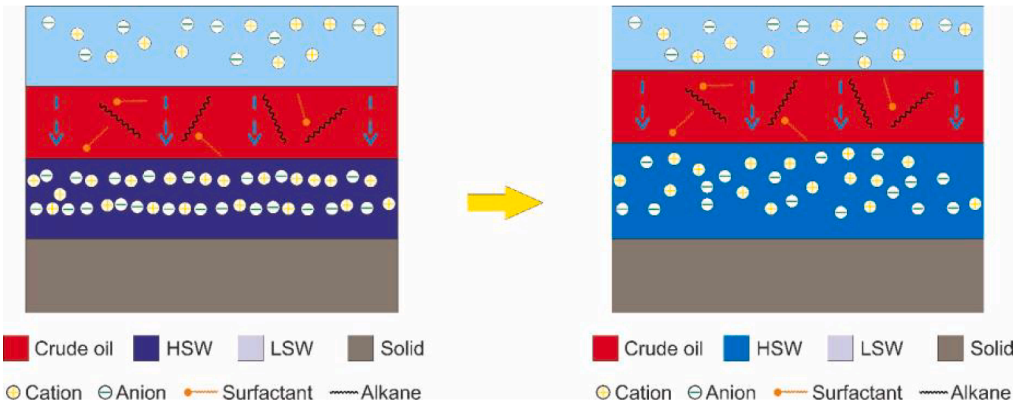

(b) water transport through oil phases before and after LSW flooding

Fig. 1. Schematic diagrams of oil motion caused by water diffusion through a water film and oil phase, respectively. (a) shows the expansion of the confined HSW layer between the oil and the solid surface. The blue arrows indicate the water transport into the HSW layer. The ion concentration is correspondingly reduced. (b) shows the expansion of the HSW layer blocked by the oil phase. The dashed arrows give the direction of water transport. The ion concentration becomes less due to the increase in water molecules. The HSW regions in both pictures have expanded due to tertiary LSW flooding and have lower ion concentrations. As a result, the confined oil regions become remobilized. (For interpretation of the references to color in this figure legend, the reader is referred to the web version of this article.)

natural surfactants. Schatzberg [41] investigated the diffusion coefficient of water in four types of hydrocarbon liquids and concluded that the solubility of water decreased with increasing molecular weight in saturated hydrocarbons. Heidman, et al. [42] found that the solubility of water in hydrocarbons is at least two orders of magnitude higher than the solubility of hydrocarbons in water, which depended on the polarizability and van der Waals interactions between the hydrocarbon and water. According to the Hildebrand solubility formula [43] salt significantly affects water activity and the solubility in hydrocarbon liquids. Presumably, higher salt concentration decreases water activity and solubility. For low-salinity flooding of a hydrocarbon reservoir, salinity in an aqueous solution would influence the water solubility and water concentration in the crude oil phase during the tertiary low-salinity waterflooding. Aldousary and Kovscek [44] reported measurements of water content in crude oil after exposing it to different salinity brines for several days. The results showed that the crude oil gained the highest water concentration when contacted with deionized water, and the concentration was about 25 times less when contacted with formation water that had an ionic strength of approximately 150,000 mg/L. Mokhtari and Ayatollahi [45] reached a similar conclusion by directly observing the dynamic change of water droplets at the crude oil/water interface with different brine samples over 45 days. Although various organic compounds, e.g., aromatics, asphaltic, etc., in crude oil might influence the movement of water molecules in oil to some extent, the salt concentration in the aqueous phase undoubtedly is a determining factor for the water solubility in oil.

From a molecular-scale perspective, molecular simulations (MD) have been employed in recent decades to study the salinity effect on the oil-water interface behavior. Such simulations are proven to be an effective tool for capturing molecular movements and further elucidating the underlying mechanisms for the transport of small molecules across a membrane, and thereby the continuum-scale transport process [46]. Marrink and Berendsen [47] performed molecular dynamics simulations on a phospholipid/water system and obtained insight into the water transport through a lipid membrane. By computing the free energy and diffusion rate profiles of water molecules across the bilayer, they determined the water permeation rate and proposed a combined solubility-diffusion model by taking the inhomogeneity of the membrane into account for describing the theoretical permeation process. Zhao, et al. [48] investigated the salinity effect on the water/n-decane interface by simulating six cases with different NaCl concentrations from 0 to 1.0 M. In their work, the simulation case with 0.2 mol NaCl yielded the minimum interfacial tension value and the maximum contact angle of a decane droplet on a water surface, which showed an optimal salinity to reach a minimum interfacial tension (IFT) value. Zhang, et al. [49] discussed the diffusion behavior of microscopic particles and their distribution at fluorobenzene-water and pentanol-water interfaces at a molecular scale. They observed that more water

molecules entered into the pentanol region with an increase in the NaCl concentration, leading to a rougher and thicker interface. Moreover, the diffusion coefficient of water molecules became lower when electrolyte ions were added to the brine. Although the effects of salinity on wettability and interfacial phenomena have been studied in depth, the oil displacement caused by water transport through hydrocarbon liquids has not been directly observed nor investigated yet via MD simulations.

In this work, to quantitively evaluate the process of water diffusion through an n-alkane phase and its contribution to the remobilization of constrained oil, we conducted a series of experiments in glass microfluidic devices with complex pore structures, mimicking the conditions at the tertiary low-salinity waterflooding process in oil reservoirs. Crude oils are customarily characterized by the type of hydrocarbon compound that is most prevalent in them: alkanes, naphthenes, and aromatics. The composition of crude oil varies depending on the geological reservoir and source. Alberta Sweet Mix Blend oil was identified to contain 281 compounds, where the n-alkane distribution shows that n-C8 to n-C17 were present in a higher concentration than other n-alkanes [50]. Our previous work [37] showed that the salinity contrast could affect the constrained crude oil movement. However, due to the complex components of crude oil, it is difficult to give a quantitative analysis and to properly distinguish the contributions of each compound to the experimental results. Therefore, we consider choosing two normal alkanes with different carbon chain lengths to present the experiments and reflect the phenomenon of water transport through oil.

The transparent micromodel provides an ideal environment to visualize dyed fluids and their behaviors in the porous medium. Before the experiments, the micromodels were treated to become hydrophobic in order to gain an oil-wet solid and prevent the formation of thin water films on the pore walls. After three rounds of fluid injection, we created multiple sandwich-like systems of LSW-alkane-HSW inside the irregular-shaped pores, shown like the distribution in Fig. 2, where the oil phase was confined between LSW and HSW. The injection procedures are explained in detail in the Section 3.2. We used three aqueous solutions (1.7 g/L LSW, 50 g/L LSW, 170 g/L HSW) together with two different alkanes (n-heptane and n-dodecane). By continuously monitoring the areas of interest for 70 h, we captured the movement of alkane/water interfaces and changes in the HSW regions. With the aid of the relevant image processing and measurement, we estimated the process of water diffusion and its contribution to the HSW swelling. Furthermore, we carried out MD simulations with three different brines to better understand the molecular mechanisms of water diffusion in the n-heptane phase due to the salinity difference. As the molecular level resolution (corresponding to nanoseconds and angstrom scales) is significantly higher than those in pore-scale experiments, MD simulations allowed us to observe the behavior of water molecules across the heptane phase at various positions that are difficult to be directly observed and analysed in pore-scale experiments.

In the following, Section 2 reviews Fick's law for describing the water solubility-diffusion through alkane phases. Then, we provide detailed descriptions of the microfluidic experiments and the microscopic optic set-up, as well as details of MD simulations in Section 3. In Section 4 the method of calculation of HSW expansion and experimental results are given and we discuss the difference between the two alkane phases. Thereafter, simulation results are shown and discussed, including the number of water molecules passing through the heptane phase and diffusion pathways. Finally, the main conclusions are summarized.

2. Theory of water diffusion through the n-alkane phase

Consider a formation initially saturated with high-salinity water and crude oil. When a tertiary low-salinity waterflood is applied to the formation, the original fluid-solid contact system of oil-HSW-rock turns into a system of LSW-oil-HSW-rock. The irregular dead-end pores will capture three types of fluids: low-salinity (bulk phase), sandwiched crude oil, and high-salinity water (connate water). In this paper, we do not consider any interaction between crude oil and water, such as emulsification, and we simplify the crude oil as a pure alkane phase. Therefore, the fluid contacts can be presented by a sandwich-like system of LSW-pure alkane-HSW, as shown in Fig. 2. When LSW (Fig. 2, left part) meets the alkane phase, the LSW-alkane interface gains more water than the HSW-alkane interface due to the higher solubility of LSW than HSW in the alkane. The diffusion coefficient for salt ions within the alkane phase is extremely low ($\sim 10^{-12}$ m^2/s), and therefore salt ions cannot easily diffuse through the alkane [44]. After dissolving, water molecules undergo a diffusive transport to move across the alkane phase from the LSW side to the HSW side and then enter the HSW region. This leads to the expansion of HSW, resulting in the increase of pressure inside the HSW and expelling constrained oil out of the dead-end pore.

The mass flux of water dissolved in oil, J_w (mole of water per unit area per time) is given by Fick's first law, $J_w = -D_w \nabla c_w$, where D_w is the diffusion coefficient of water in oil and c_w is the molar concentration of water. For cases that the solute molecule is smaller than the solvent, the diffusion coefficient can be approximately calculated by the modified Stokes-Einstein equation, $D_w = \frac{k_B T}{6\pi\eta^{0.78} r}$, where k_B is Boltzmann's constant ($m^2 \bullet kg \bullet s^{-2} \bullet K^{-1}$), T is the absolute temperature (K), η is the shear viscosity of the solvent ($kg \bullet m^{-1} \bullet s^{-2}$) and r is the radius of the solute (m) [51,52]. Under stationary conditions, the flux of water through the alkane phase in the direction of the concentration gradient can be approximated as

$$J_{w,x} = -D_w \frac{\partial c_w}{\partial x} = D_w \frac{c_{LSW} - c_{HSW}}{\Delta x} \quad (1)$$

where c_{LSW} and c_{HSW} are the water concentrations in the oil at the LSW-alkane and HSW-alkane interfaces, respectively, and Δx is the distance between these two interfaces. As mentioned in the Introduction, the ionic strength can strongly impact the water concentration in the crude oil phase [44,45]. The relationship is not linear, meaning that there is an optimal salt concentration leading to the lowest water content [37]. The exact relationship of water solubility in n-alkane versus salinity is barely studied in the literature, which causes a challenge to calculate the

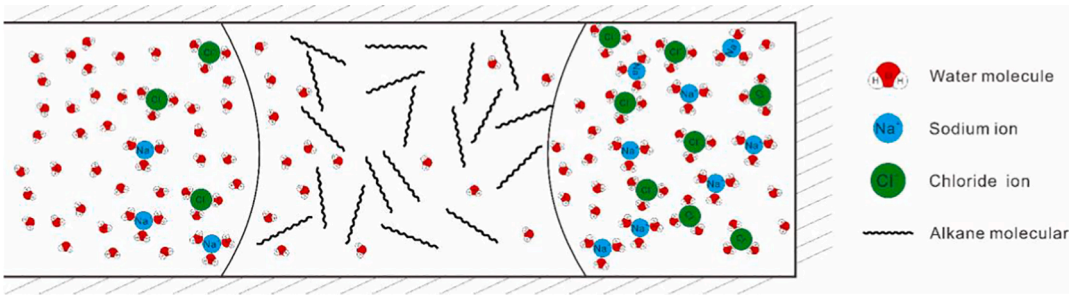

Fig. 2. A schematic diagram of water transport in the n-alkane phase via diffusion in one system of LSW-alkane-HSW formed in one dead-end pore. The left part and right part present low-salinity water region and high-salinity water region, respectively. The pore surface is assumed to be oil wet.

accurate water mass flux in an alkane. To quantify the water volumetric flux and mass flux, a series of microfluidic experiments have been conducted. In Section 4, by measuring the area change of trapped HSW in our experiments, we estimate a relationship between salinity and water volumetric flux.

3. Microfluidic experiments and molecular simulation details

3.1. Observation setup and micromodel information

To obtain the direct pore-scale visualization of fluid behavior, we build an optic setup using an Olympus SZX7 Zoom Stereo Microscope and a 9-megapixel UC90 digital camera (Fig. 3a). The microscope has a magnification range of 8x to 56x. The camera allows us to obtain color images with a high resolution of ~0.83 μm/pixel. The micro-chip holder is placed on the manually driven stage on the microscope platform. A dual-drive system syringe pump, Harvard Apparatus Pump 33 DDS, is used for fluid injection into the microchip for mimicking the low-salinity waterflooding process in an oil reservoir. The quasi-2D microchip is provided by Micronit Technologies B.V., the Netherlands. The pore network of the microchip (Fig. 3b) has a domain of 10 mm (width) ×20 mm (length), with a permeability of 2.5 Darcy and a porosity of 57%. Note that the porosity and permeability are expected not to affect on the water transport through oil phase in the pore space of micro-chips. It is made of borosilicate glass and designed with random grain structures (white areas in the figure) to represent the rock shape in one slice of sandstone. Anisotropic acid etching method is applied to achieve the pore spaces with a uniform depth of 20 μm.

To avoid the formation of water-thin films on the pore walls, we rendered the wettability of micro-chips from naturally water-wet to oil-wet. A siliconizing fluid, 1,7-Dichloro-1,1,3,3,5,5,7,7-Octamethyltetrasiloxane, was used for this purpose. The procedure, similar to the procedure used in Arab, et al. [53], is briefly explained below.

- Dilute the siliconizing fluid in heptane to make a 1% v/v solution.
- Sequentially inject the solution, heptane, and methanol into a dry and clean microfluidic chip with an injection rate of 50 μL/min for 5 min each.
- Dry the chip in the oven at 80 °C for 24 h.

After treatment, the chip surface renders to strongly oil-wet with a water contact angle of ≈97° and a dodecane contact angle of ≈17°. The measurements of contact angles are shown in Fig. 4. Therefore, we assumed that there were no thin water films along the grain surfaces and no water flux through corners. Moreover, our previous work [37] in glass-based capillary has demonstrated that there was no fluorescent water film generated along the capillaries, either with hydrophilic capillaries or hydrophobic capillaries.

3.2. Fluid preparation and injection procedures

We prepared four types of fluids for our experiments: low-salinity water, high-salinity water, n-heptane, and n-dodecane. High-salinity water (brine) was synthetically made by mixing deionized water and different amounts of four pure salts to produce a ≈170 g/L solution: NaCl, Na_2SO_4, $MgCl_2{\cdot}6H_2O$, and $CaCl_2 \bullet 2H_2O$. All chemicals were purchased from Sigma Aldrich. The composition of high-salinity brine is listed in Table 1. Then, we diluted the HSW either 100 times or 3.4 times to obtain two low salinity brines of 1.7 g/L LSW and 50 g/L LSW, respectively. Two kinds of n-alkane with different hydrocarbon chain lengths, n-heptane (C_7H_{16}) and n-dodecane ($C_{12}H_{26}$), were selected as the oil.

To clearly distinguish the three phases under the camera, we dyed the low-salinity brine and oil with two different chemicals, methylene blue, and Sudan red, respectively. Note that both dyes have strong staining functions, so only a small amount is required to achieve the staining effect, which does not affect the salinity concentration or fluid properties of the alkenes. Methylene blue made the 1.7 g/L LSW and 50 g/L HSW appear blue under the microscope. Oil was tinted brown by Sudan red, a yellowish-red dye. No dye was added to the 170 g/L high salinity brine, which remained transparent. Thereafter, we always filtered the dyed solution to remove undissolved dye particles and prevent pore clogging.

For placing the LSW-alkane-HSW system inside a microchip, we first vacuumed all the air in a wettability-modified and dry microchip, then saturated it with high-salinity water considered as connate water. Subsequently, the alkane phase, i.e., heptane or dodecane, was injected at a rate of 100 μL/min to displace most of the HSW out of the microchip. With this relatively high injection rate, not all of HSW could be displaced by the injected oil, and a residual HSW remained in the microchip. Next, LSW was injected at a rate of 5 μL/min (around 0.4 ft/day) to flush out most of the oil. The injection was stopped when the LSW breakthrough occurred. We waited 30 min to allow fluid distribution inside the microchip to become stable. Finally, the inlet and outlet valves were shut to avoid external interference. This injection procedure allowed us to obtain multiple sandwich-like clusters of LSW-alkane-HSW in the irregular-shaped pores. Due to imaging limitations, we had to choose an area of interest to maximize the resolution when observing an individual LSW-alkane-HSW cluster. To acquire the change of water-oil interfaces, the observed area was continuously monitored for at least 48 h at room temperature. Overall, two sets of experiments were carried out: one with pure n-heptane and another with pure n–dodecane. Next to these, two

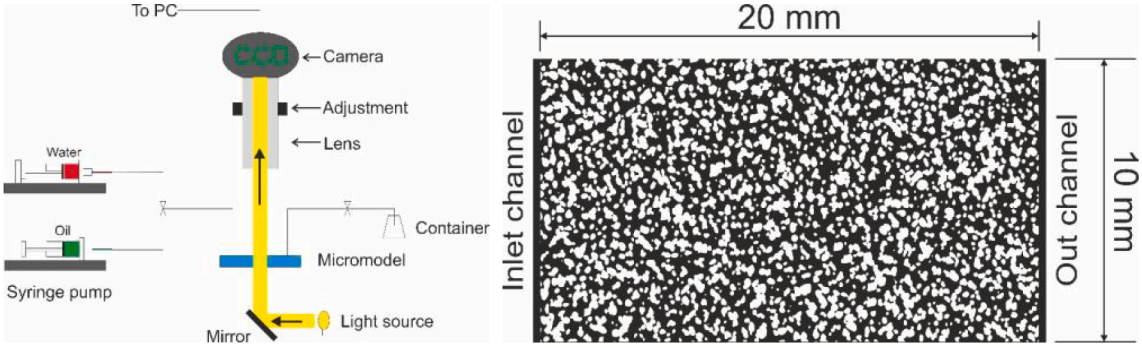

(a) observation setup **(b) a photomask of microchip**

Fig. 3. The schematic picture of observation setup (a) and a design of the microchip (b). The white areas in (b) represent the grain structures, while black areas are the pore space and inlet/outlet channels.

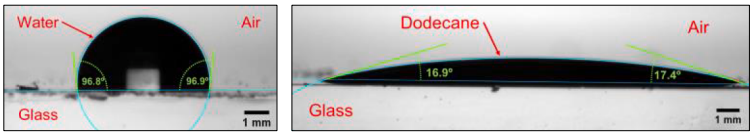

(a) water contact angle (b) dodecane contact angle

Fig. 4. Pictures of contact angle on the modified glass micro-chips.

Table 1
Chemical composition of high-salinity brines at ambient conditions.

Ion	Compound added	Mol. Weight (g/mole)	HSW Concentrations (mg/L)
Na^+	NaCl	58.44	50,374
Ca^{2+}	$CaCl_2 \bullet 2H_2O$	146.8	10,983
Mg^{2+}	$MgCl_2{\cdot}6H_2O$	203.1	1586
SO_4^{2+}	Na_2SO_4	142.04	234
Cl^-			109,181
TDS*			172,358

* Total dissolved solids.

reference experiments were performed without a salinity contrast, where the injected and initial water solutions both had a salinity of 1.7 g/L. Various experiments are listed in Table 2. Each experiment was repeated at least twice to check the reproducibility.

3.3. Estimation of water flux into the alkane phase

From the images of an LSW-alkane-HSW cluster in the microchips, we can obtain direct information on the width of the alkane phase, the contact areas of LSW-alkane and HSW-alkane, and volume changes of HSW and LSW. Here we relate the water mass flux through the oil to the change of volume of HSW. To obtain comparable results in water flux in different experiments, we need a method for normalizing the water diffusion flux for different phase geometries. The schematic geometry of an LSW-alkane-HSW system is shown in Fig. 5. As the confined alkane commonly has irregular geometry, we consider the water diffusion only in the direction of the minimum thickness of oil, denoted by d_{oil}, and use this distance as the length of water transport through the oil from the LSW to the HSW. We assume that the water transport through the oil phase occurs over an average cross-sectional area $A^c_{ave} = hL_{ave}$, where h is the height of the pores in the micro-fluidics chip and L_{ave} is the average of lengths of HSW-alkane and LSW-alkane interfaces. Thus, the water mass flux through an oil meniscus can be also approximated as:

$$\int_{A^c_{ave}} J_w dA \simeq \overline{J}_w h L_{ave} = D_w \frac{c_{LSW} - c_{HSW}}{d_{oil}} h L_{ave} \tag{2}$$

Next, consider the rate of volume increase of the HSW region, Q_w. This can be written as:

$$Q_w = \frac{dV_{HSW}}{dt} = h\frac{dA_{HSW}}{dt} \tag{3}$$

where A_{HSW} is the observed planar area of HSW. The right-hand side of Eq. (2) is equal to the right of Eq. (3) multiplied by water density, ρ_w:

Table 2
List of experiments conducted in micro-chips.

Exp. No	Alkane type	Resident water	Flooding solution	Info.
1	n-heptane	HSW (170 g/L)	LSW (1.7 g/L)	
2		HSW (170 g/L)	LSW (50 g/L)	
3		LSW (1.7 g/L)	LSW (1.7 g/L)	reference
4	n-dodecane	HSW (170 g/L)	LSW (1.7 g/L)	
5		HSW (170 g/L)	LSW (50 g/L)	
6		LSW (1.7 g/L)	LSW (1.7 g/L)	reference

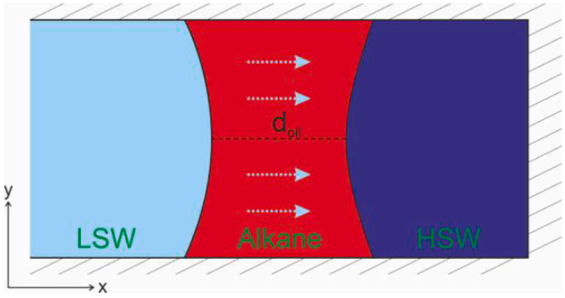

Fig. 5. Schematic representation of an LSW-alkane-HSW system. The direction of water mass flux diffusing through one alkane phase is shown by light blue arrows. (For interpretation of the references to color in this figure legend, the reader is referred to the web version of this article.)

$$D_w \frac{c_{LSW} - c_{HSW}}{d_{oil}} L_{ave} = \rho_w \frac{dA_{HSW}}{dt} \tag{4}$$

Using Eq. (4), the water mass flux in two alkanes with different salinity contrast, $D_w(c_{LSW} - c_{HSW})/d_{oil}$, can be evaluated. To compare the water volumetric flux for different cases, we define reference parameters as: $t_{ref} = \frac{d_{oil}A_0}{D_w L_{ave}}$, and $Q_{ref} = hA_0/t_{ref}$, where A_0 is the initial area of HSW. The corresponding dimensionless forms can be given as, $A^* = A_{HSW}/A_0$, $t^* = t/t_{ref}$, and $Q^* = \frac{Q_w}{Q_{ref}} = \frac{d_{oil}}{D_w L_{ave}} \frac{dA_{HSW}}{dt}$. In the next section, we will show the HSW area change, water mass flux for individual observed regions, and plot the function of dimensionless volumetric flux versus dimensionless time. The error of area measurement is 3%. From the literature [52], we find the diffusion coefficients of water in heptane and dodecane are $7.4 \pm 0.75 \times 10^{-9}$ m^2/s and $3.0 \pm 0.27 \times 10^{-9}$ m^2/s. Furthermore, the concentration difference between LSW-alkane interface and HSW-alkane interface, $(c_{LSW} - c_{HSW})$, is able to be estimated, which allows us to compare the rate of concentration change $\Delta c/c_{w0}$ with the increase rate of HSW area $\Delta A_{HSW}/A_{H0}$, where c_{w0} and A_{w0} are the initial water concentration at LSW-alkane interface and initial HSW area, respectively. We assume the initial water concentration is the solubility of pure water in alkanes. Here the values are 0.091 g/L and 0.065 g/L for heptane and dodecane, respectively, given by the literature [43].

3.4. Molecular dynamic model and simulation details

In order to explore the water salinity effect on water transport across an oil film and the resulting alkane remobilization at a pore-scale, a simulation system consisting of the major ingredients used in experiments was designed. The dimension of the system is shown in Fig. 6. All MD simulations were carried out using the LAMMPS package [54]. The visualization and analysis were implemented by the OVITO software [55]. Specifically, pure water (PW) and saline water (SW) were set on the two sides of a layer of oil phase (pure heptane). The system was assigned periodic boundary conditions. However, in order to guarantee the differences in salinity at two sides of the oil phase, graphene layers were used as separators on the z-direction at both ends of the simulation box, like many previous studies [56–58]. The graphene layers would not affect the interactions of water molecules with the oil phase due to the

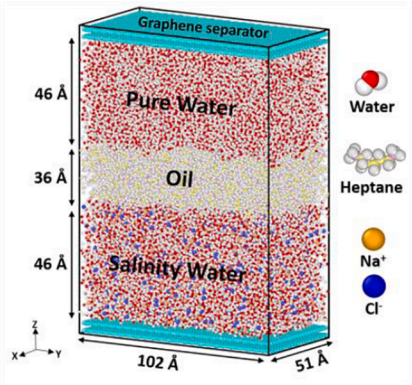

Fig. 6. Simulation system and the structures of the molecular components.

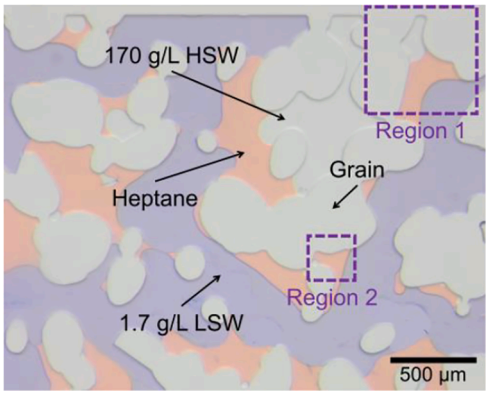

Fig. 7. The observed domain in experiment No.1, where the oil phase was pure n-heptane. The dashed squares are the selected regions for quantifying the HSW area change.

cut-off distance. The oil phase had a thickness of 36 Å covering the whole cross-sectional area of the simulation box (102×51 Å^2). The density of the oil phase was calibrated to match experimental measurements [59,60]. In total, the system contained 705 heptane molecules and 16,374 water molecules (half on each side). The Na^+ and Cl^- ion concentration in one of the water layers was chosen so as to correspond with the experiments in this work, namely with the concentration of 0%, 5%, and 20%. Thus, three types of systems with ion concentration differences between two water-solution layers of 0%-0%, 0%-5%, and 0%-20% were modeled.

The Optimized Potentials for Liquid Simulations All-Atom (OPLS-AA) force field was applied for heptane molecules [61], and the simple point charge (SPC) model was used to describe water molecules [62]. Na^+ and Cl^- ions were modeled using the Leonard-Jones parameters derived by Aluru et al. [63]. Leonard-Jones potential (LJ 12–6) and the Coulomb potential were employed to describe the non-bonded interaction and the electrostatic interaction, respectively, as defined by Eq. (5) below:

$$V_{non-bonded} = 4\varepsilon_{ij}\left[\left(\frac{\sigma_{ij}}{r_{ij}}\right)^{12} - \left(\frac{\sigma_{ij}}{r_{ij}}\right)^{6}\right] + \frac{q_i q_j}{4\pi\varepsilon_0 r_{ij}} \quad (5)$$

where ε_{ij} and σ_{ij} denote the energy well depth and van der Waals radius, and q_i were the atomic charge of atom i. Arithmetic mixing rule was adopted to calculate LJ potentials between species i and j. The cut-off distance was 12 Å. For long-range electrostatic interactions, the particle-particle particle-mesh (PPPM) method was chosen [64]. The force field parameters for all atoms were given in Table SI-1 in the supporting materials.

For all simulations, the graphene separators were position fixed as the solid wall. The rest of the system was first energy-minimized using the steepest descent method and subsequently subjected to equilibration under the NVT ensemble. The time step used in the simulation was 1 fs. The temperature of the system was fixed to 340 K using the Nosé–Hoover thermostat with a damping coefficient of 100 fs [65]. The equilibration time of the system was 1 ns. Five independent simulations were carried out for each system, each with a simulation length of 46 ns. The trajectory of the simulation was collected every 10000 fs during the simulation for the analysis of water diffusion and mass transport in the system.

4. Results and discussion

4.1. Microfluidic experiment with n-heptane

In this part, we will discuss the results of experiments No.1-No.3 (see Table 2) with the pure n-heptane. In none of the experiments with alkane, emulsification was observed. The observed domain of experiment No.1 was continuously monitored for 70 h (Fig. 7). The bulk phase of 1.7 g/L LSW was recognized by its bluish color. The light grey areas were the solid grains and the connate of water 170 g/L HSW was transparent. The interface between the grains and the HSW was visible as darker lines. The HSW was trapped by the wetting phase heptane. Light brown areas showed the heptane phase confined between low-salinity water and high-salinity water. The color of HSW and the grains are identical, but we can easily filter out the areas of the grain by using the micromodel mask in image analysis. The dashed squares represented the two regions selected for detailed analysis, which showed relatively isolated LSW-oil-HSW clusters.

Fig. 8 shows the change of HSW area of Region 1 during 70 h of monitoring. Information on Region 2 is provided in the supplementary materials and plotted in Fig. 9. We observed a significant swelling of the HSW area during the experiment. The curvature of the HSW water-alkane interface gradually increased, indicating the change of capillary pressure between the HSW and the oil. The distance between the HSW and LSW interfaces decreased during the observation period.

By measuring the area of HSW and the oil area (shown in Fig. 9a), we noticed that the HSW areas in Region 1 and Region 2 grew by 119.4% and 261.3%, respectively, during the 70 h of observation, while the heptane areas in both regions remained nearly unchanged. With the strong oil-wet microchip, we assumed that there were no thin water films on the surface of the grains. Therefore, the increase in HSW area was attributed to water passing through the heptane region only. We plotted the water mass flux J_w for two regions at six different times, as shown in Fig. 9b. There was a slight difference between the two regions because of the different oil thickness d_{oil}. The average water mass flux for the two regions was 1.7×10^{-7} kg/(m^2 • s). The corresponding concentration difference of water at two water-oil interfaces was presented in Fig. 9c and displayed a slow downward trend with the increase in time. This means the water solubility difference was reduced as a result of the dilution in HSW regions, which supports the hypothesis we proposed in Section 2, namely water diffusion through the n-alkane phase due to the solubility difference of water at two interfaces of water-alkane. The water volumetric flux enters the trapped HSW between oil and solid grain and causes its volume increase, resulting in the pressure increase inside the HSW and the constrained oil relocation. The averaged water solubility difference for two observed regions was about 2.7×10^{-3} g/L. Moreover, the plot of $\Delta c/c_{w0}$ versus $\Delta A_{HSW}/A_{H0}$ (see inset in Fig. 9c) shows that the reduction in the concentration difference was not a linear function of increased HSW area. This was found in other experiments as well.

To evaluate the effect of salt concentration, the concentration of LSW was increased to 50 g/L in experiment No.2. Detailed information of the observed domain can be found in Section 2 of the supplementary document. The changes of heptane area and HSW area over 70 h of monitoring are shown in Fig. 10a. The measurements indicated that the

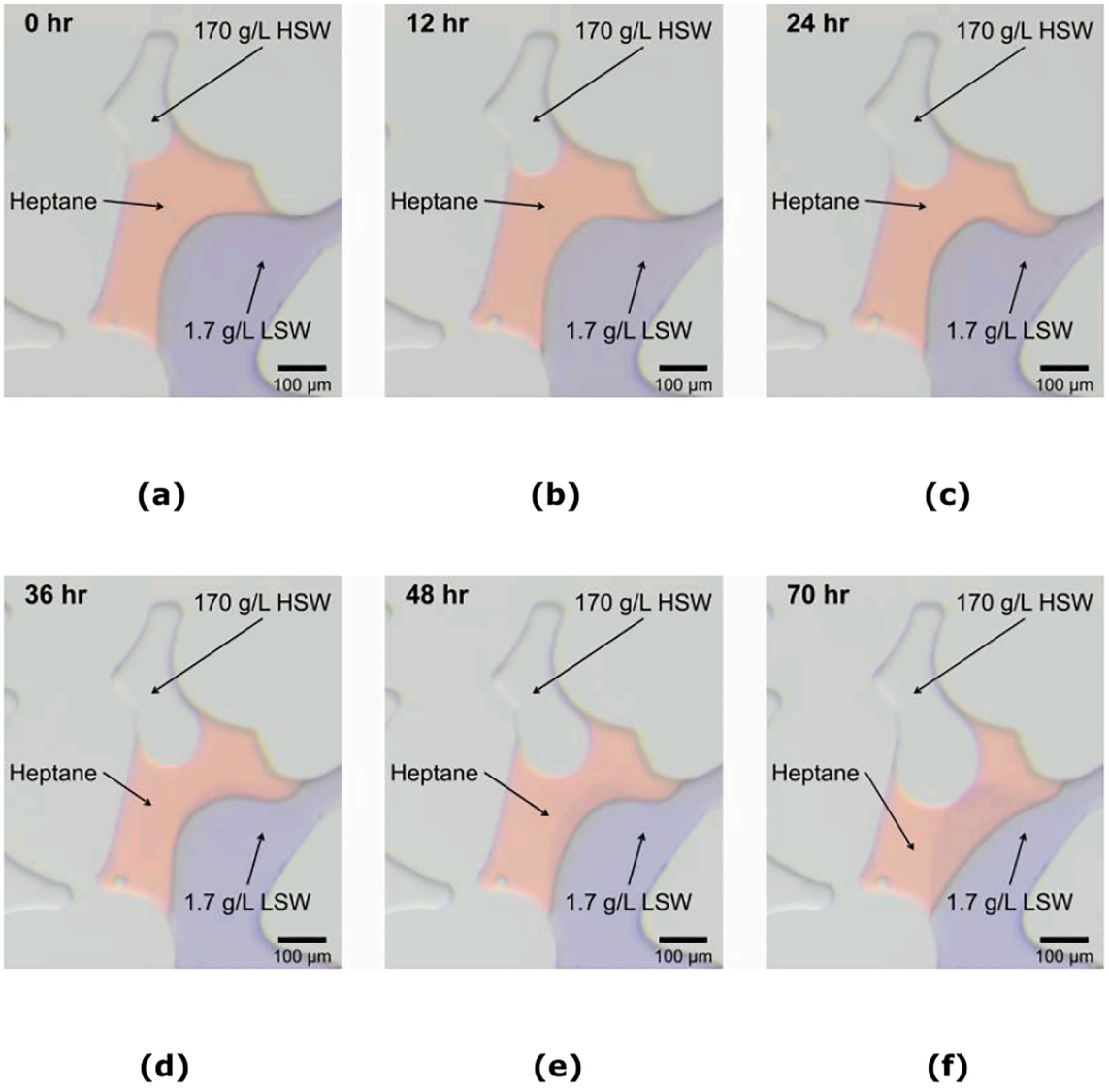

Fig. 8. Images of the isolated LSW-heptane-HSW cluster in Region 1 at six different times from 0 to 70 h. The bluish area presents 1.7 g/L LSW as the bulk phase. Heptane is shown in brown, and 170 g/L HSW is confined by heptane and solid surfaces.

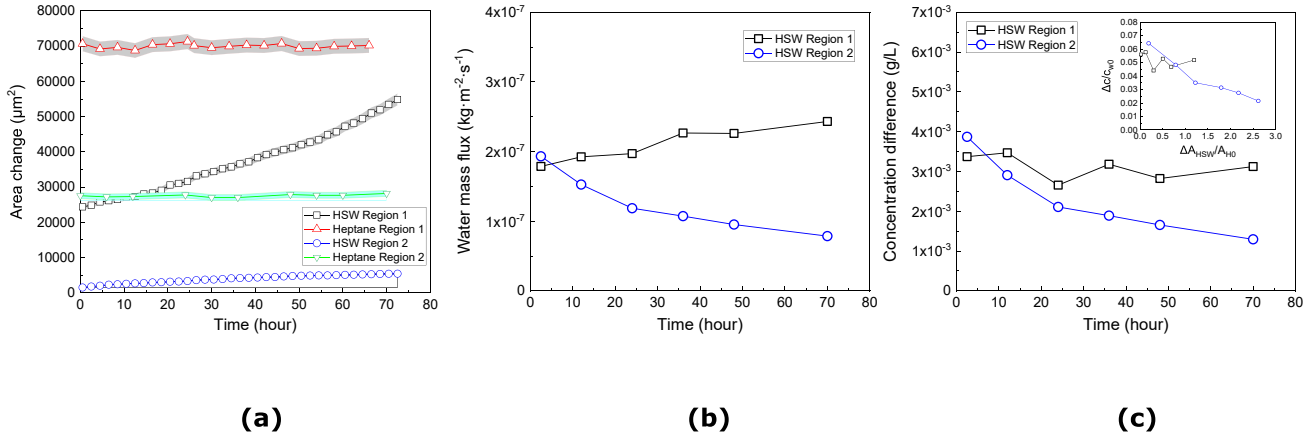

Fig. 9. Results of area changes in Region 1 and Region 2, for the case of LSW having a salt concentration of 1.7 g/L. (a) The area changes of heptane and HSW in the two regions for 70 h. The measurement error is indicated in the shadow band. (b) The water mass flux as a function of time. (c) The water concentration difference between LSW-heptane interface and HSW-heptane interface. The inset figure presents a relationship between the water concentration change and the HSW area change.

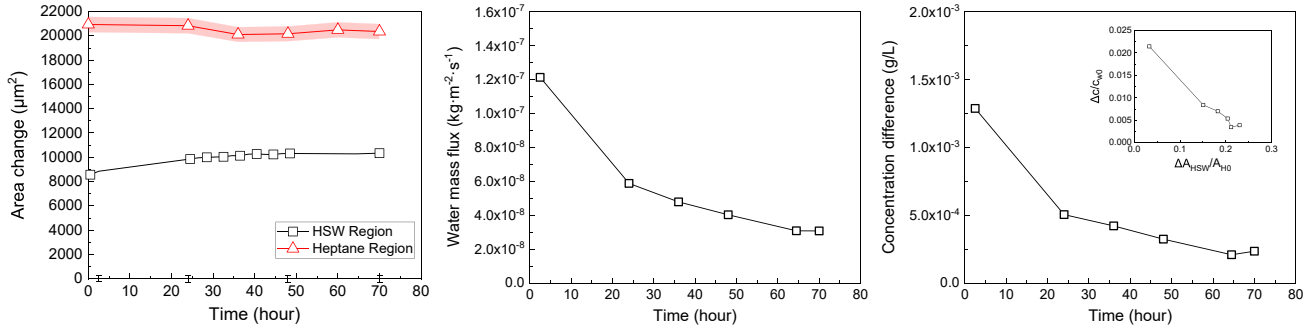

Fig. 10. Results of observations of heptane and HSW, for the case of LSW having a salt concentration of 50 g/L. (a) This figure shows the area changes of heptane and HSW for 70 h. The measurement error is indicated in the shadow band. (b) This figure shows the water mass flux as a function of time. (c) This figure shows the change of water concentration difference between LSW-heptane interface and HSW-heptane interface. The inset presents a relationship between water concentration change and HSW area change.

HSW area had a slight swelling, reaching a plateau after about 30 h, and eventually increased by 20.7% after 70 h, while oil region area remained relatively constant. The increase of HSW area was much less than in experiment No.1. The results of water mass flux at six moments are shown in Fig. 10b. The trend presented that at the first 24 h, water mass flux in heptane decreased rapidly by 51.8%, but after 36 h it levelled off. Correspondingly, concentration differences of water at two water-alkane interfaces (presented in Fig. 10c) showed a dramatic drop then gradually decreased. The inset figure shows the non-linear relationship between water solubility change and HSW area change as well.

In the baseline experiment No.3, where connate and injected water had equal salinity of 1.7 g/L, we did not observe significant changes in the water and heptane areas, indicating that a low-ionic environment without a salinity contrast did not induce water transport through oil and oil motion. The images are presented in Section 3 of the supplementary document.

4.2. Microfluidic experiments with n-dodecane

In order to investigate the influence of hydrocarbon length on water diffusion, we chose n-dodecane as another alkane solution and conducted experiments No.4-No.6 with the same procedures as in the previous experiments. In experiment No.4 with 1.7 g/L LSW and 170 g/L HSW, two regions were selected to study changes in HSW and oil clusters in detail; see Fig. 11.

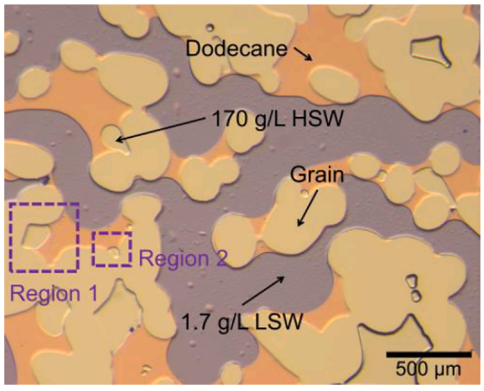

Fig. 11. The observed domain in experiment No.4 with pure n-dodecane. The blue dashed squares are the selected regions for quantifying the HSW area change. (For interpretation of the references to color in this figure legend, the reader is referred to the web version of this article.)

The zoomed images of Region 1 during 70 h of monitoring are shown in Fig. 12. The individual images for Region 2 are given in the supplementary materials. We see that Region 1 had a significant increase in HSW area, like the experiments with heptane. The interface of HSW-dodecane increased, and the distance between HSW and LSW gradually decreased. Based on the area measurements, see Fig. 13a, we found that the HSW area of Region 1 grew by 41.2% after 70 h, while oil areas did not have an obvious change. The water mass fluxes at six moments are plotted in Fig. 13b, showing that the two HSW regions had very close values of water mass fluxes in dodecane and the same variation trend. Fig. 13c shows the concentration differences of water in dodecane for two regions and the non-linear relationship between concentration change and area change. The concentration differences kept reducing during 70 h, which was caused by the continuous dilution of HSW and the rise in water concentration at the HSW-dodecane interface.

Experiment No.5, with 50 g/L LSW and 170 g/L HSW, was performed to investigate the effect of salinity on the water penetration through dodecane. Images of the observed domain and the selected region can be found in Section 5 of the supplementary document. The area change of HSW, water mass flux through dodecane and water concentration difference are plotted in Fig. 14. As the behavior of HSW area was very similar to the behavior in the No.2 experiment, we did not explain the swelling phenomenon in HSW area, the tendency of water mass flux, and the change in concentration difference. The reference experiment, where both water phases were 1.7 g/L LSW, indicated that there was no significant change of trapped connate water. The images are shown in Section 6 of the supplementary document.

4.3. Effect of hydrocarbon length and salinity

In order to compare the water volumetric flux for different cases, we calculated the dimensionless form versus dimensionless time, shown in Fig. 15. In all cases, the water volumetric flux was relatively high at the beginning and then rapidly declined until reaching low levels at the later stage. The results indicated that water diffused through both alkanes and the flux is strongly affected by the salinity contrast at two sides of alkane. Regarding the salinity effect, a salinity contrast of 1.7 g/L-170 g/L caused higher water volumetric fluxes in both alkanes than 50 g/L-170 g/L. Notably, the difference in volumetric flux between 1.7 g/L and 50 g/L was not proportional to the salinity contrast, which reflected the effect of salinity on the water solubility in alkanes. The continuously diluting HSW area caused a changing water solubility at the HSW-alkane interface, leading to the non-linear change of water concentration difference between two interfaces of alkanes. However, water volumetric flux through dodecane was higher than through heptane but it had a

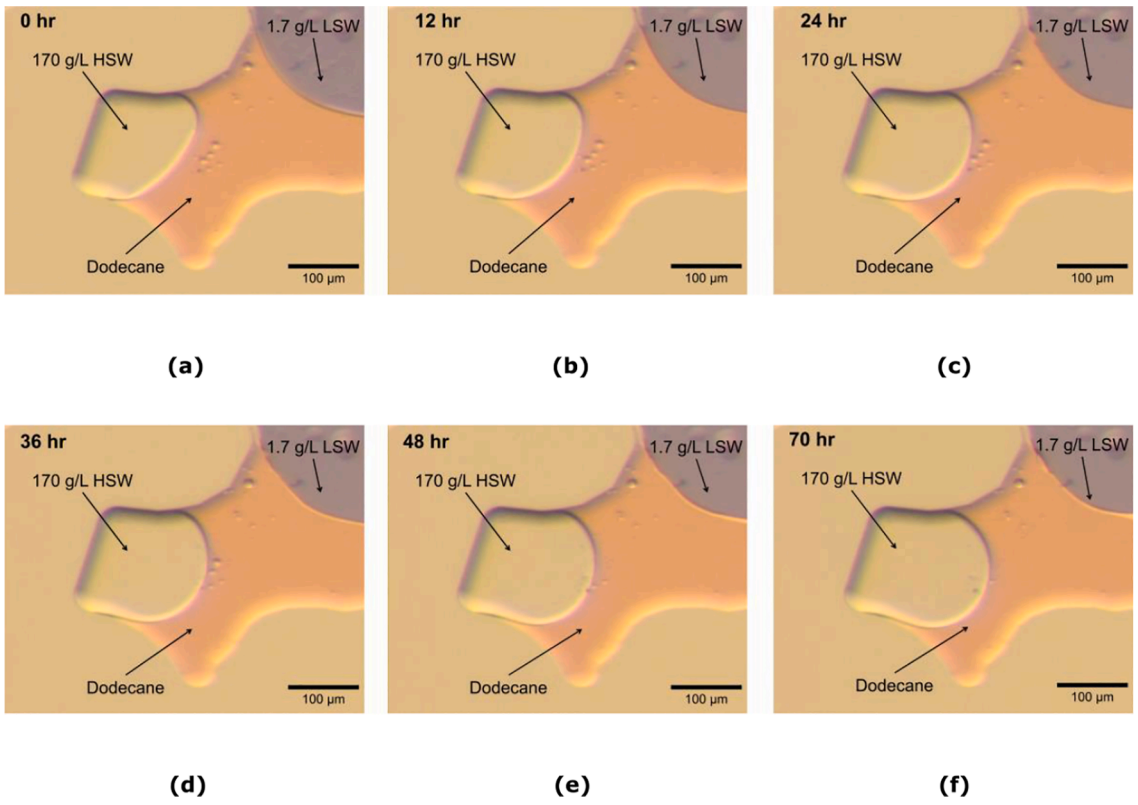

Fig. 12. Images of an LSW-dodecane-HSW system at six different times from 0 to 70 h. The bluish area presents 1.7 g/L LSW as the bulk phase. Dodecane is shown in brown, and we observe changes in the transparent 170 g/L HSW confined by dodecane and solid surfaces.

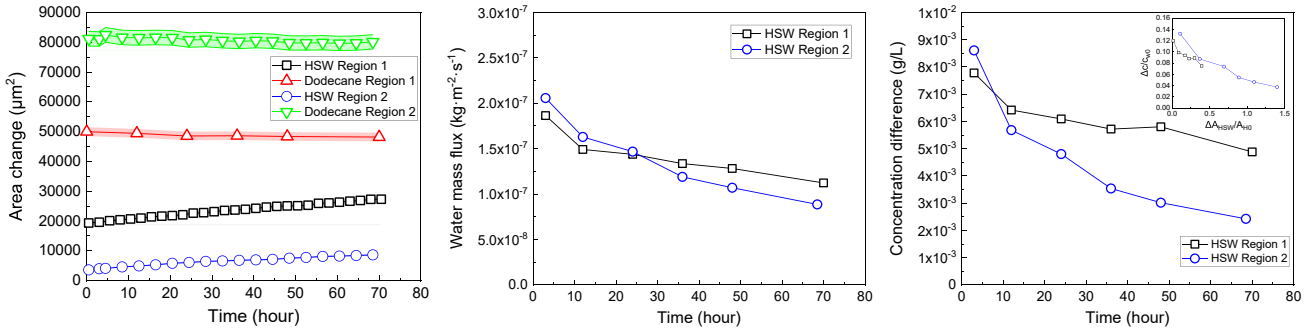

Fig. 13. Results of observations of dodecane and HSW in Region 1 and Region 2, for the case of LSW having a salt concentration of 1.7 g/L. (a) Area changes of dodecane and HSW as a function of time. The measurement error is presented by the shadow band. (b) The water mass flux as a function of time. (c) The change of water concentration difference between LSW-dodecane interface and HSW-dodecane interface. The inset presents a relationship between water concentration change and HSW area change.

faster drop at the initial period ($t^*<25$). After $t^*>50$, dodecane and heptane had closer water volumetric fluxes, which reflected that the salinity had a different influence on the water solubility in different alkane phases. However, it is difficult to find a simple relationship between the chain length of hydrocarbon and water volumetric flux. This would require more experiments and data involving more types of alkanes. In the next section, we will show results of molecular dynamics simulations of the salinity effect on diffusion of water molecules through heptane and give a qualitative observation of water transport at a molecular scale.

4.4. *Molecular scale water diffusion*

Diffusion of water molecules across the oil phase were captured by molecular dynamic (MD) simulations. Results corroborates experimental observations. As seen from the diffusing trajectory, shown in Fig. 16a, a fraction of water molecules from the pure water (PW) phase can migrate through the oil phase into the saline water (SW) phase. Movement of a water molecule across the oil phase was a random and rare event in the simulations. Typically, a water molecule sampled the PW phase for a significantly long simulation time, and by chance swiftly diffused through the oil layer into the SW phase (Fig. 16a). For obtaining a quantitative net inflow of water molecules, the changes in the number

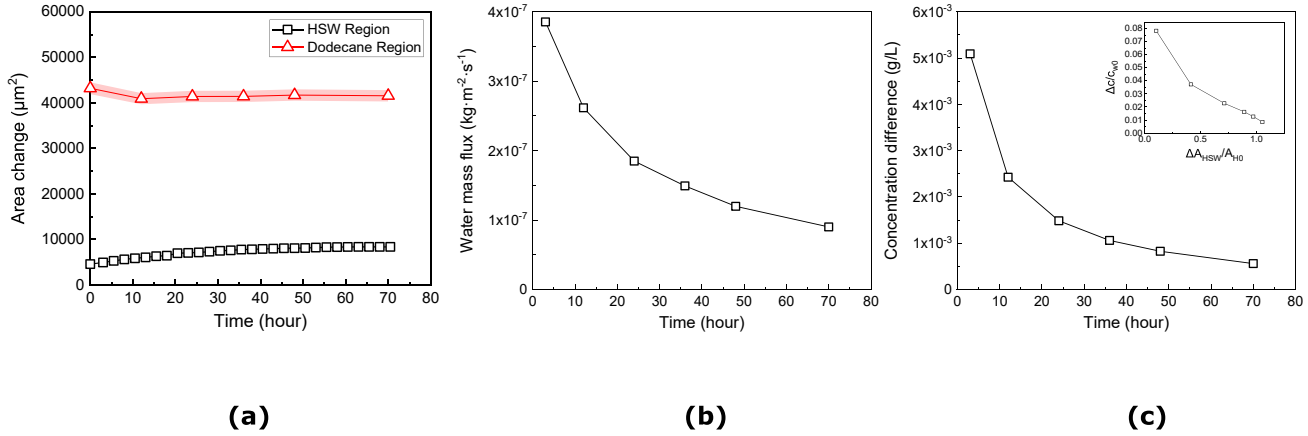

Fig. 14. Results of observations of dodecane and HSW for the case of LSW having a salt concentration of 50 g/L. (a) Area changes of dodecane and HSW as a function of time. The measurement error is presented by the shadow band. (b) The water mass flux as a function of time. (c) The change of water concentration difference between LSW-dodecane interface and HSW-dodecane interface. The inset presents a relationship between water concentration change and HSW area change.

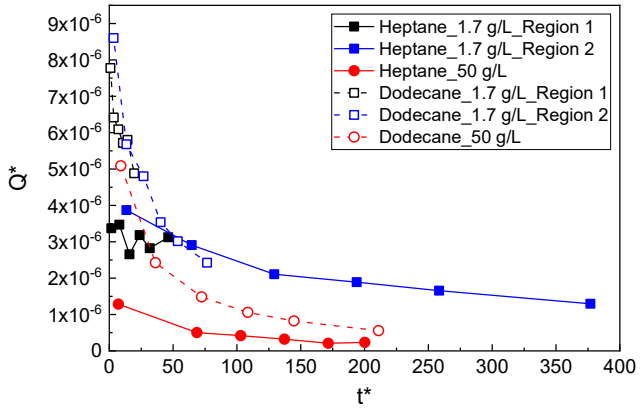

Fig. 15. The results of water volumetric flux in alkane phases for all experiments. Three solid curves represent the water volumetric flux in heptane with 1.7 g/L LSW for two regions and 50 g/L HSW for one region. The three dashed curves show the results for dodecane cases.

of water molecules in and out of the SW phase were monitored in the simulations. As shown in Fig. 16b and Fig. SI9, the net inflow of water molecules were significantly different among the three model systems that were already introduced in Section 3. For the system with two pure water phases (0%-0%), no obvious net inflow was observed between the two PW phases, meaning there was no obvious statistical directionality in water migration across the oil phase. For a higher salinity in the SW phases of 5% and 20% NaCl, net inflow of water molecules toward the PW phase was identified, with the threshold increasing the ion concentration in the SW phase (Fig. 16b). During the whole simulation, no ion was monitored diffused through the oil phase. Such results strongly suggested a correlation between water diffusion preferences and the ion concentration differences in the system and provided atomic-scale validation to the findings in the microfluidic experiments. It should be noted here that the oil phase used in the simulation system was orders of magnitude thinner than in experiments for the purpose of revealing water diffusion in the oil phase in a feasible simulation time. Water diffusion through the oil phase in experiments should require a much longer time in reality.

Water molecules diffused through the oil phase in the system need to cross two interfaces. The nature of the oil-water interface played a key role in the net inflow of water migration. The average equilibrium

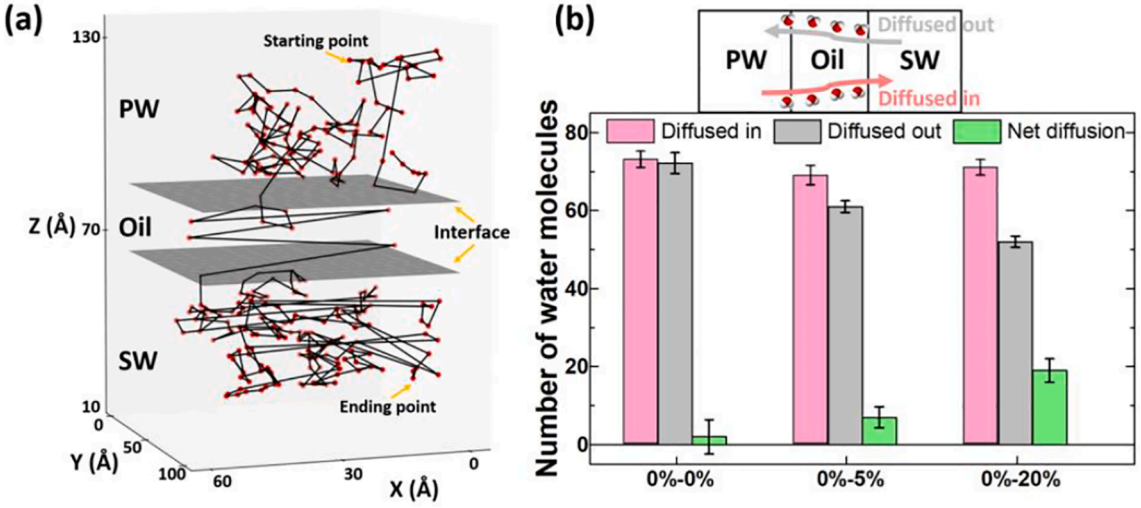

Fig. 16. Water diffusion across the oil phase and net diffusion in the systems. (a) A typical migration trajectory of a water molecule across the oil phase (the abrupt steps of trajectory in the oil phase resulted from the periodic boundary condition of the simulation box.). (b) Comparison of net diffusion of water molecules into the SW phase in the three model systems.

densities of different components along the z-direction of the system in the early stage of the simulations were characterized to investigate the structure of the interface. As the density profiles of the systems plotted in Fig. 17a and Fig. SI10 show, the density values of both pure water and heptane agree well with experimental values (around 1.0 g/cm^3 and 0.68 g/cm^3, respectively). With the addition of ions, the water density in the SW was slightly lower than the PW phase (Fig. 17a), due to the effects of volume exclusion and structural coordination of ions on the nearby water molecules as observed in other studies [66,67]. Here, both sodium and chloride ions might undergo hydration reactions and surrounding shells of water molecules were obviously formed, as snapshots shown in Fig. 17a. Furthermore, each system contained two well-defined interfaces between oil and the two water solutions, due to the immiscibility of the water and oil molecules. The average of interfacial thickness and interfacial tension of each interface was determined by the ion concentration, as seen from results given in Fig. 17b. The interfacial thickness was calculated here using the 90–90 criterion [68], namely the distance between two lines, where the local density is equal to 90% of the respective bulk value (the blue region highlighted in Fig. 17b). The interfacial tension, γ, was calculated from the following equation [69]:

$$\gamma = \frac{1}{2}L_z[p_{zz} - \frac{1}{2}(p_{xx} + p_{yy})] \quad (6)$$

where L_z is the length of the simulation domain in the z-direction; p_{xx}, p_{yy}, p_{zz} are the stress tensor components in the x, y, and z directions, respectively. More detailed information on the calculation is given in Section SI-10. The calculated interfacial tension for the heptane/water interface is around 49.8 mN/m, which agreed well with the experimental value of 50.1 mN/m [70]. The results indicated that higher salinity led to higher interfacial tension, and at the same time lower interfacial thickness. The dependence of both interfacial tension and thickness was in line with observations in previous studies [48,71,72]. Such dependence can be attributed to the strong electrostatic force induced by ions in the solution, where water molecules strongly bound to the ions and restrained the tendency of migration to the interface. Therefore, higher salinity led to a lower miscibility of SW and heptane. Lower salinity contrast also resulted in a reduction of probability of water diffusion through the interface into the oil phase, which drove the net inflow of water molecules from PW into SW (Fig. 16b).

The salinity also significantly affected water diffusion. Water diffusion can be quantitatively characterized by water molecular mean square displacement (MSD) in the three systems with various salinity, which are shown in Fig. 17c. The water molecular diffusion coefficient (D) was evaluated using the following equation:

$$D = \frac{1}{6}\lim_{t\to\infty}\frac{dMSD}{dt} \quad (7)$$

The diffusion coefficient of water molecules in PW (pure water) phase in all systems was found to be around 5.16 ± 0.39 μm^2/ms, matching well with values by experiments and other simulations (5–5.5 μm^2/ms) [73,74]. With the increasing salinity, the diffusion coefficient decreased significantly, yielding values of ± 0.28 and 2.98 ± 0.27 μm^2/ms for systems with 5% and 20% salinity, respectively. Higher salinity resulted in slower water diffusion. Such results were expected, as the attraction of ions to water molecules and the formation of hydrated ions, on the one hand, hindered the diffusion of water molecules and, on the other hand, decreased the number of free molecules in the system. The result was also consistent with the analysis of changes in the interface structure. Therefore, the existence of hydrated ion structure not only affects the migration of water molecules but also weakens their solubility in oil at the oil-water interface. This effect resulted in a lower solubility of water in oil in the SW side, which drives the phenomenon of directional net flow of water towards the high salinity water (as described in Fig. 16b).

4.5. Future works

In this paper, we have systematically studied water diffusion through two pure alkane phases and its effect on oil movement. However, one point that needs to be studied is the salinity effect of other alkanes and

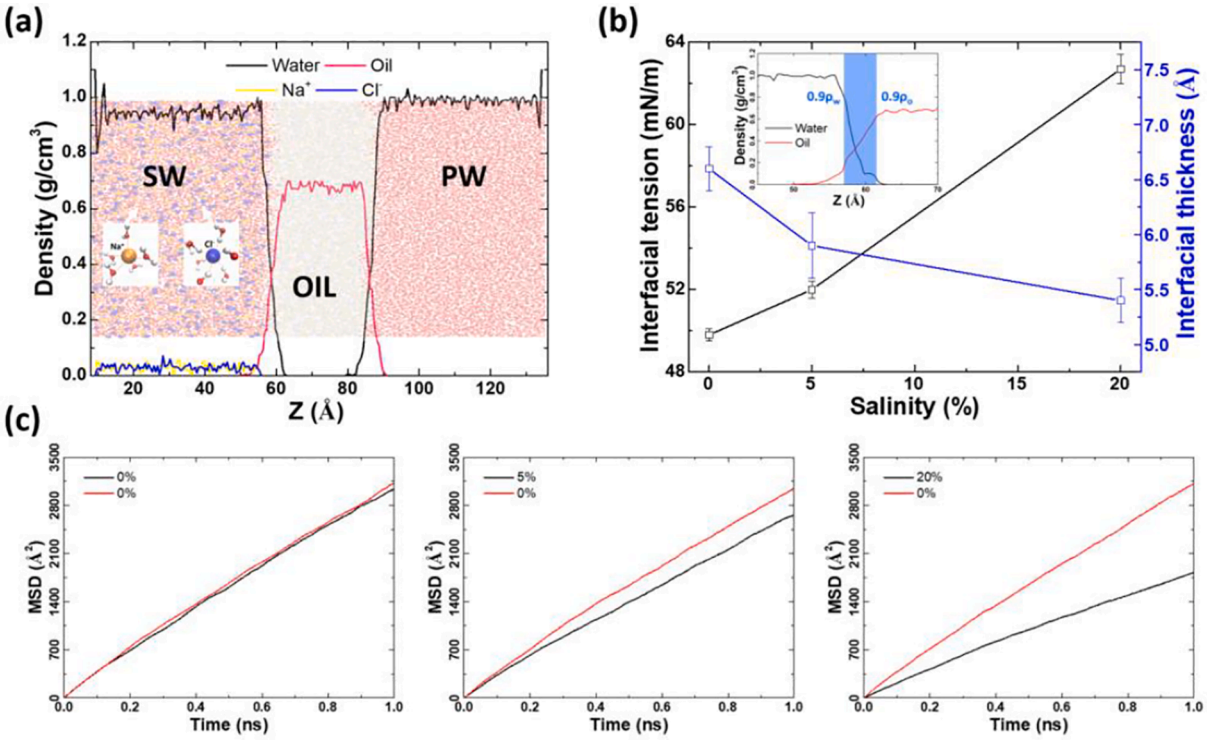

Fig. 17. Molecular scale water dynamics. (a) Density profiles of the major components in the 0%-oil-20% system. (b) Profiles of interfacial tension and thickness in the 0%-oil-20% system. (c) The representative change of mean square displacement (MSD) of water molecules with time in three different water solution phases.

real crude oil. Note that the contribution of water diffusion through oil phase to final oil recovery is still questionable. Other mechanisms, e.g., wettability alteration, multi-component ion exchange, and double-layer expansion, are also debatable and play crucial roles in enhanced oil recovery. We also believe natural surfactants that are present in crude oil, such as the asphaltenes composed of polyaromatic carbon rings, can form microemulsion within oil near the low-salinity water-oil interface, and form an additional driving force for the diffusion of water toward the high-salinity water. The microemulsion size and distribution may be highly influenced by the salt concentration [45]. Therefore, our further investigations are to conduct microfluidic experiments involving surfactants in the alkane phases and to describe the emulsion movement under salinity contrast using MD simulations. In addition, the water diffusion into the oil phase could be enhanced at elevated temperatures such as those under reservoir conditions because of the faster movement of water molecules. The temperature effects should be further explored in future studies.

5. Summary and conclusions

In summary, this study focused on providing a better understanding of the water transport processes occurring in porous oil reservoirs, which affect oil movement during low-salinity water flooding. The hypothesis of water diffusion through the oil phase induced by the solubility difference was expounded, and the oil was dislodged and is thus available for remobilization. To mimic the low-salinity water flooding in an oil reservoir, two series of microscopic experiments were conducted to establish a sandwich-like system of LSW-oil-HSW in hydrophobic micro-chips. We noted that for both hydrocarbons the HSW areas significantly increased when there was a salinity contrast with the LSW. In contrast, there was no visible change in the reference experiments that HSW and LSW had no salinity difference. The features of water diffusion were assessed for two pure hydrocarbons at the microscopic scale. Moreover, to advance our insights into the behavior of water molecules in the alkanes, molecular dynamic (MD) simulations were performed with three cases of NaCl concentration difference across an oil film of heptane. We described the trajectory of water diffusion through heptane from low-salinity water to high-salinity water, investigated the statistical results of dynamic net inflow of water molecules into HSW, and determined interfacial tension and the diffusion coefficients of water in heptane for the various salinity systems. By combining the pore-scale experiments and molecular-scale modeling, we draw the following conclusions.

- Water is capable to diffuse through the studied alkane phases, i.e., heptane and dodecane, due to a salinity contrast, which causes the expansion of disconnected high-salinity water and displacement of constrained oil. Using osmosis theory only cannot fully explain water transport in the oil phase and the HSW expansion during low-salinity water flooding.
- Ionic strength and the hydrocarbon chain length both play important roles in water diffusion. Heptane and dodecane both were found to be diffusive to water, and this property could be significantly affected by the salinity contrast at two sides of alkanes. A salinity contrast of 1.7 g/L-170 g/L caused a higher water volumetric flux in both alkanes than 50 g/L-170 g/L. Dodecane showed a higher diffusivity to water but a faster drop at the initial period ($t^*<25$) than heptane. After the period of $t^*>50$, dodecane and heptane had closer water volumetric fluxes. However, it was difficult to conclude that there was a simple relationship between the chain length of hydrocarbon and water diffusivity.
- For both alkanes, the difference in water volumetric flux between the case of 1.7 g/L- 170 g/L and the case of 50 g/L-170 g/L were not proportional to the salinity contrast during the experimental period. We hypothesized that the continuously diluting HSW domain caused a changing water solubility at the HSW-alkane interface, leading to the non-linear change of water concentration difference across the alkane phase.
- Through conducting MD simulation, we observed water molecules transported through the heptane phase and a higher number of water molecules passed the water-heptane interface driven by ion concentration differences. There was a net flux of water molecules towards the high salinity water. Meanwhile, based on the calculated profiles of ions, almost no ions appear at the oil-water interface and inside the heptane phase. Sodium ions and chloride ions underwent hydration reactions with surrounding water molecules to form a structure of hydrated ions.
- By investigating the interfacial tension changes and mean square displacement (MSD) calculations, we conclude that higher salinity leads to a lower diffusion coefficient of water molecules (around 4.48 and 2.98 $\mu m^2/ms$ for 5% and 20%, respectively), i.e., slower water movement. Moreover, high salinity reduces the probability of water diffusion through the interface into the oil phase. This leads to lower solubility of water in oil near the oil-HSW interface and thus verifies the experimental result that the direction of net water movement is towards high salinity water.

Declaration of Competing Interest

The authors declare that they have no known competing financial interests or personal relationships that could have appeared to influence the work reported in this paper.

Acknowledgements

We would like to acknowledge Wenyu Zhou and Mohammad Hossein Golestan for experimental support with the microfluidics experiments. Author Lifei Yan acknowledges the support from China Scholarship Council (No. 201609120013). This work is financially supported by the Research Council of Norway (Grant No. 234626) and the Chinese Scholarship Council (No. 201908320254). The supercomputer CPU hours were provided by the Norwegian Metacenter for Computational science (Project ID: NN9110K and NN9391K). The third author (SMH) wishes to thank the German Research Foundation (DFG) for supporting this work by funding – EXC2075 – 390740016 under Germany's Excellence Strategy and acknowledge the support by the Stuttgart Center for Simulation Science (SimTech). Author Carl Fredrik Berg was supported by the Research Council of Norway through its Centers of Excellence funding scheme (project number 262644, PoreLab).

Appendix A. Supplementary data

Supplementary data to this article can be found online at https://doi.org/10.1016/j.fuel.2022.124716.

References

[1] Morrow N, Buckley J. Improved oil recovery by low-salinity waterflooding. J Petrol Technol 2011;63(05):106–12.
[2] Hua Z, Li M, Ni X, Wang H, Yang Z, Lin M. Effect of injection brine composition on wettability and oil recovery in sandstone reservoirs. Fuel 2016;182:687–95.
[3] W. Alameri, T. W. Teklu, R. M. Graves, H. Kazemi, and A. M. AlSumaiti, "Wettability alteration during low-salinity waterflooding in carbonate reservoir cores." In *SPE Asia Pacific Oil & Gas Conference and Exhibition*. 2014. Society of Petroleum Engineers.
[4] Mahmud HB, Mahmud WM, Arumugam S. Numerical investigation of optimum ions concentration in low salinity waterflooding. Advances in Geo-Energy Research 2020;4(3):271–85.
[5] S. Erke *et al.* "Low salinity flooding trial at west Salym field." In *SPE Improved Oil Recovery Conference*. 2016. Society of Petroleum Engineers.
[6] P. McGuire, J. Chatham, F. Paskvan, D. Sommer, and F. Carini. "Low salinity oil recovery: An exciting new EOR opportunity for Alaska's North Slope." In *SPE western regional meeting*, 2005: Society of Petroleum Engineers.
[7] G. Thyne and P. Gamage. "Evaluation of the effect of low salinity waterflooding for 26 fields in Wyoming." In *SPE Annual Technical Conference and Exhibition*. 2011. OnePetro.

[8] Katende A, Sagala F. A critical review of low salinity water flooding: mechanism, laboratory and field application. J Mol Liq 2019;278:627–49.
[9] Al-Shalabi EW, Sepehrnoori K. A comprehensive review of low salinity/engineered water injections and their applications in sandstone and carbonate rocks. J Petrol Sci Eng 2016;139:137–61.
[10] Bartels W-B, Mahani H, Berg S, Hassanizadeh S. Literature review of low salinity waterflooding from a length and time scale perspective. Fuel 2019;236:338–53.
[11] Tang G-Q, Morrow NR. Influence of brine composition and fines migration on crude oil/brine/rock interactions and oil recovery. J Petrol Sci Eng 1999;24(2–4):99–111.
[12] Buckley J, Liu Y, Monsterleet S. Mechanisms of wetting alteration by crude oils. SPE J 1998;3(01):54–61.
[13] Y. Zhang and N. R. Morrow. "Comparison of secondary and tertiary recovery with change in injection brine composition for crude-oil/sandstone combinations." In *SPE/DOE symposium on improved oil recovery*. 2006. Society of Petroleum Engineers.
[14] Austad T. "Water-based EOR in carbonates and sandstones: New chemical understanding of the EOR potential using "Smart Water"," in *Enhanced oil recovery Field case studies*. Elsevier 2013:301–35.
[15] A. Lager, K. J. Webb, C. Black, M. Singleton, and K. S. Sorbie. "Low salinity oil recovery-an experimental investigation1." *Petrophysics*. 49. 01. 2008.
[16] D. J. Ligthelm, J. Gronsveld, J. Hofman, N. Brussee, F. Marcelis, and H. van der Linde. "Novel Waterflooding Strategy By Manipulation Of Injection Brine Composition." In *EUROPEC/EAGE conference and exhibition*. 2009. Society of Petroleum Engineers.
[17] A. Emadi and M. Sohrabi. "Visual investigation of oil recovery by low salinity water injection: formation of water micro-dispersions and wettability alteration." In *SPE annual technical conference and exhibition*. 2013. 30. Society of Petroleum Engineers.
[18] K. Sandengen and O. Arntzen. "Osmosis during low salinity water flooding." In *IOR 2013-17th European Symposium on Improved Oil Recovery*. 2013.
[19] Zhang T, Li Y, Cai J, Meng Q, Sun S, Li C. A digital twin for unconventional reservoirs: A multiscale modeling and algorithm to investigate complex mechanisms. Geofluids 2020;2020.
[20] Schmatz J, Urai JL, Berg S, Ott H. Nanoscale imaging of pore-scale fluid-fluid-solid contacts in sandstone. Geophys Res Lett 2015;42(7):2189–95.
[21] Joekar-Niasar V, Mahani H. Nonmonotonic pressure field induced by ionic diffusion in charged thin films. Ind Eng Chem Res 2016;55(21):6227–35.
[22] Mahani H, Berg S, Ilic D, Bartels W-B, Joekar-Niasar V. Kinetics of low-salinity-flooding effect. SPE J 2015;20(01):8–20.
[23] Aseyednezhad S, Yan L, Hassanizadeh SM, Raoof A. An accurate reduced-dimension numerical model for evolution of electrical potential and ionic concentration distributions in a nano-scale thin aqueous film. Adv Water Resour 2022;159:104058.
[24] W.-B. Bartels, H. Mahani, S. Berg, R. Menezes, J. van der Hoeven, and A. Fadili, "Low salinity flooding (LSF) in sandstones at pore scale: micro-model development and investigation," in *SPE Annual Technical Conference and Exhibition*, 2016: Society of Petroleum Engineers.
[25] Song R, Peng J, Sun S, Wang Y, Cui M, Liu J. Visualized experiments on residual oil classification and its influencing factors in waterflooding using micro-computed tomography. J Energy Res Technol 2020;142(8):083003.
[26] Wei B, Zhang X, Liu J, Xu X, Pu W, Bai M. Adsorptive behaviors of supercritical CO2 in tight porous media and triggered chemical reactions with rock minerals during CO2-EOR and-sequestration. Chem Eng J 2020;381:122577.
[27] Belhaj AF, et al. Experimental investigation, binary modelling and artificial neural network prediction of surfactant adsorption for enhanced oil recovery application. Chem Eng J 2021;406:127081.
[28] Sandengen K, Kristoffersen A, Melhuus K, Jøsang LO. Osmosis as mechanism for low-salinity enhanced oil recovery. SPE J 2016;21(04):1227–35.
[29] P. Mahzari and M. Sohrabi, "Crude oil/brine interactions and spontaneous formation of micro-dispersions in low salinity water injection," in *SPE improved oil recovery symposium*, 2014: Society of Petroleum Engineers.
[30] Wu T, Firoozabadi A. Surfactant-Enhanced Spontaneous Emulsification Near the Crude Oil-Water Interface. Langmuir 2021;37(15):4736–43.
[31] Kar T, Cho H, Firoozabadi A. Assessment of low salinity waterflooding in carbonate cores: Interfacial viscoelasticity and tuning process efficiency by use of non-ionic surfactant. J Colloid Interface Sci 2022;607:125–33.
[32] Rücker M, et al. From connected pathway flow to ganglion dynamics. Geophys Res Lett 2015;42(10):3888–94.
[33] Ayirala SC, Al-Yousef AA, Li Z, Xu Z. Water ion interactions at crude-oil/water interface and their implications for smart waterflooding in carbonates. SPE J 2018;23(05):1817–32.
[34] Fredriksen S, Rognmo A, Sandengen K, Fernø M. Wettability effects on osmosis as an oil-mobilization mechanism during low-salinity waterflooding. Petrophysics 2017;58(01):28–35.
[35] Crestel E, Kvasničková A, Santanach-Carreras E, Bibette J, Bremond N. Motion of oil in water induced by osmosis in a confined system. Phys Rev Fluids 2020;5(10):104003.
[36] Du Y, Xu K, Mejia L, Zhu P, Balhoff MT. Microfluidic Investigation of Low-Salinity Effects During Oil Recovery: A No-Clay and Time-Dependent Mechanism. SPE J 2019.
[37] Yan L, Aslannejad H, Hassanizadeh SM, Raoof A. Impact of water salinity differential on a crude oil droplet constrained in a capillary: Pore-scale mechanisms. Fuel 2020;274:117798.
[38] Lakshminarayanaiah N, White M. "Water flow through polymeric and nonaqueous liquid membranes," *Journal of Polymer Science Part A-1*. Polym Chem 1969;7(8):2235–45.
[39] Sanahuja-Embuena V, Lim S, Górecki R, Trzaskus K, Hélix-Nielsen C, Shon HK. Enhancing selectivity of novel outer-selective hollow fiber forward osmosis membrane by polymer nanostructures. Chem Eng J 2021:133634.
[40] Li W, Nan Y, You Q, Jin Z. CO2 solubility in brine in silica nanopores in relation to geological CO2 sequestration in tight formations: Effect of salinity and pH. Chem Eng J 2021;411:127626.
[41] P. Schatzberg, "Diffusion of water through hydrocarbon liquids," in *Journal of Polymer Science Part C: Polymer Symposia*, 1965, vol. 10, no. 1: Wiley Online Library, pp. 87-92.
[42] Heidman J, Tsonopoulos C, Brady C, Wilson G. High-temperature mutual solubilities of hydrocarbons and water. Part II: Ethylbenzene, ethylcyclohexane, and n-octane. AIChE J 1985;31(3):376–84.
[43] Schatzberg P. Solubilities of water in several normal alkanes from C7 to C161. The Journal of Physical Chemistry 1963;67(4):776–9.
[44] Aldousary S, Kovscek AR. The diffusion of water through oil contributes to spontaneous emulsification during low salinity waterflooding. J Petrol Sci Eng 2019;179:606–14.
[45] Mokhtari R, Ayatollahi S. Dissociation of polar oil components in low salinity water and its impact on crude oil–brine interfacial interactions and physical properties. Pet Sci 2019;16(2):328–43.
[46] MacElroy J, Boyle M. Nonequilibrium molecular dynamics simulation of a model carbon membrane separation of CH4/H2 mixtures. Chem Eng J 1999;74(1–2):85–97.
[47] Marrink S-J, Berendsen HJ. Simulation of water transport through a lipid membrane. The Journal of Physical Chemistry 1994;98(15):4155–68.
[48] Zhao J, Yao G, Ramisetti SB, Hammond RB, Wen D. Molecular dynamics simulation of the salinity effect on the n-decane/water/vapor interfacial equilibrium. Energy Fuels 2018;32(11):11080–92.
[49] Zhang C, Dai H, Lu P, Wu L, Zhou B, Yu C. Molecular Dynamics Simulation of Distribution and Diffusion Behaviour of Oil-Water Interfaces. Molecules 2019;24(10):1905.
[50] Wang Z, Fingas M, Li K. Fractionation of a light crude oil and identification and quantitation of aliphatic, aromatic, and biomarker compounds by GC-FID and GC-MS, part II. J Chromatogr Sci 1994;32(9):367–82.
[51] Hynes JT, Kapral R, Weinberg M. Molecular theory of translational diffusion: Microscopic generalization of the normal velocity boundary condition. J Chem Phys 1979;70(3):1456–66.
[52] Su JT, Duncan PB, Momaya A, Jutila A, Needham D. The effect of hydrogen bonding on the diffusion of water in n-alkanes and n-alcohols measured with a novel single microdroplet method. J Chem Phys 2010;132(4):044506.
[53] Arab D, Kantzas A, Torsæter O, Akarri S, Bryant SL. A Crucial Role of the Applied Capillary Pressure in Drainage Displacement. SPE J 2021:1–19.
[54] Plimpton S. Fast parallel algorithms for short-range molecular dynamics. J Comput Phys 1995;117(1):1–19.
[55] Stukowski A. Visualization and analysis of atomistic simulation data with OVITO–the Open Visualization Tool. Modell Simul Mater Sci Eng 2009;18(1):015012.
[56] Yan Y, Wang W, Li W, Loh K, Zhang J. A graphene-like membrane with an ultrahigh water flux for desalination. Nanoscale 2017;9(47):18951–8.
[57] Wang P, et al. CO2/N2 separation via multilayer nanoslit graphene oxide membranes: molecular dynamics simulation study. Comput Mater Sci 2017;140:284–9.
[58] Li W, et al. Molecular dynamics simulations of CO2/N2 separation through two-dimensional graphene oxide membranes. The Journal of Physical Chemistry C 2016;120(45):26061–6.
[59] Aminabhavi T, Patil V, Aralaguppi M, Phayde H. Density, viscosity, and refractive index of the binary mixtures of cyclohexane with hexane, heptane, octane, nonane, and decane at (298.15, 303.15, and 308.15) K. J Chem Eng Data 1996;41(3):521–5.
[60] Patterson J, Morris E. Measurement of absolute water density, 1 C to 40 C. Metrologia 1994;31(4):277.
[61] Jorgensen WL, Maxwell DS, Tirado-Rives J. Development and testing of the OPLS all-atom force field on conformational energetics and properties of organic liquids. J Am Chem Soc 1996;118(45):11225–36.
[62] Berendsen H, Grigera J, Straatsma T. The missing term in effective pair potentials. J Phys Chem 1987;91(24):6269–71.
[63] Joung IS, Cheatham III TE. Determination of alkali and halide monovalent ion parameters for use in explicitly solvated biomolecular simulations. J Phys Chem B 2008;112(30):9020–41.
[64] Hockney RW, Eastwood JW. Computer Simulation using Particles. CRC Press; 2021.
[65] Nosé S. A molecular dynamics method for simulations in the canonical ensemble. Mol Phys 1984;52(2):255–68.
[66] Badizad MH, Koleini MM, Hartkamp R, Ayatollahi S, Ghazanfari MH. How do ions contribute to brine-hydrophobic hydrocarbon Interfaces? An in silico study. J Colloid Interface Sci 2020;575:337–46. https://doi.org/10.1016/j.jcis.2020.04.060.
[67] Koleini MM, Mehraban MF, Ayatollahi S. Effects of low salinity water on calcite/brine interface: A molecular dynamics simulation study. Colloids Surf, A 2018;537:61–8. https://doi.org/10.1016/j.colsurfa.2017.10.024.
[68] Xu J, et al. Effect of surfactant headgroups on the oil/water interface: An interfacial tension measurement and simulation study. J Mol Struct 2013;1052:50–6.
[69] Y. Chang, S. Xiao, R. Ma, X. Wang, Z. Zhang, and J. He. "Displacement dynamics of trapped oil in rough channels driven by nanofluids." *Fuel*. 122760. 2021.
[70] B. Kumar. "Effect of salinity on the interfacial tension of model and crude oil systems." Graduate Studies. 2012.

[71] Underwood TR, Greenwell HC. The water-alkane interface at various Nacl salt concentrations: a molecular dynamics study of the readily available force fields. Sci Rep 2018;8(1):1–11.
[72] Paul S, Chandra A. Hydrogen bond dynamics at vapour–water and metal–water interfaces. Chem Phys Lett 2004;386(4–6):218–24.
[73] Tsimpanogiannis IN, Moultos OA, Franco LF, Spera MBdM, Erdős M, Economou IG. Self-diffusion coefficient of bulk and confined water: a critical review of classical molecular simulation studies. Mol Simul 2019;45(4–5):425–53.
[74] Easteal AJ, Price WE, Woolf LA. Diaphragm cell for high-temperature diffusion measurements. Tracer diffusion coefficients for water to 363 K. J Chem Soc, Faraday Trans 1 F 1989;85(5):1091–7.